Article

Enhanced deep Southern Ocean stratification during the lukewarm interglacials

Huang Huang [1,2,3,4] ✉, Jan Fietzke [5], Marcus Gutjahr [5], Martin Frank [5], Gerhard Kuhn [6], Xu Zhang [7], Claus-Dieter Hillenbrand [7], Dengfeng Li [3,4], Jingyan Hu [3] & Jimin Yu [1,8]

Between ~800 and 430 thousand years ago lukewarm interglacials were characterized by lower atmospheric CO_2 levels and colder Antarctic temperatures than subsequent interglacials. The Southern Ocean is thought to have played a crucial role, but associated ocean circulation changes remain poorly constrained, at least in part, due to the scarcity of proxy data. By using a novel 2D laser ablation technique, we here provide the first orbital-resolution Southern Ocean seawater Pb isotope records over the past 800 thousand years from a ferromanganese crust located at mid-depth (~1.6 km water depth) on Antarctica's Pacific margin. Our results reveal systematically higher $^{208}Pb/^{206}Pb$ ratios during lukewarm interglacials than during more recent interglacials while $^{206}Pb/^{204}Pb$ ratios remained similar, suggesting reduced vertical deepwater mixing in the Southern Ocean during lukewarm interglacials. By enhancing deep-sea carbon sequestration and thereby lowering atmospheric CO_2, strengthened deep Southern Ocean stratification likely imposed critical impacts on the lukewarm interglacial climates.

Compared to more recent periods, interglacial atmospheric CO_2 concentrations and Antarctic air temperatures were lower during the period between 800 and 430 thousand years ago (ka), commonly referred to as the "lukewarm interglacials"[1,2]. The shift to warmer interglacials at ~430 ka, known as the Mid-Brunhes Event (MBE)[3] or Mid-Brunhes Transition (MBT)[4], marks a key change in the Earth's climate history.

The Southern Ocean (SO) is a critical region where carbon- and nutrient-rich deep waters are upwelling, causing enhanced surface ocean productivity and driving substantial carbon exchange between the deep ocean and the atmosphere[5,6]. In addition to upwelling, the SO is also a key region of Antarctic Bottom Water (AABW) formation (downwelling), which regulates ocean-atmosphere carbon exchange[7].

As such, the SO has been identified as an important region controlling atmospheric CO_2 and climate dynamics across the MBE[8–12]. Mechanisms proposed to explain lower CO_2 during the lukewarm interglacials include increased AABW production[8,12], northward shifts of SO fronts[13] and weakened SO upwelling[11], all of which involve changes in basin-scale deep ocean circulation. However, reconstructions of SO circulation during the lukewarm interglacials remain scarce, in particular for regions south of the Antarctic Polar Front (APF) where key processes like AABW formation and upwelling take place.

Reconstructing past SO circulation is particularly challenging due to the lack of carbonate sediments from this region, which restricts the availability of reliable age data (based on ^{14}C and $\delta^{18}O$) and limits the use of traditional paleo water mass tracers such as $\delta^{13}C$ and Cd/Ca

[1]Laoshan Laboratory, Qingdao, China. [2]Laboratory for Marine Geology, Qingdao Marine Science and Technology Center, Qingdao, China. [3]School of Marine Sciences, Sun Yat-Sen University, Zhuhai, Guangdong, China. [4]Southern Marine Science and Engineering Guangdong Laboratory (Zhuhai), Zhuhai, Guangdong, China. [5]GEOMAR Helmholtz Centre for Ocean Research Kiel, Kiel, Germany. [6]Alfred-Wegener-Institut Helmholtz-Zentrum für Polar- und Meeresforschung, Bremerhaven, Germany. [7]British Antarctic Survey, High Cross, Madingley Road, Cambridge, UK. [8]SKLLQG, Institute of Earth Environment, Chinese Academy of Sciences, Xi'an, China. ✉e-mail: huang17323@gmail.com

signatures in carbonate tests (shells) of fossil foraminifera. Additionally, other water mass tracers, such as seawater neodymium (Nd) and lead (Pb) isotopes, preserved in sediments are susceptible to alteration and contamination from high influxes of chemically immature glacial detritus from the Antarctic margin[14,15].

In this study, we reconstruct SO circulation changes using radiogenic Pb isotope records from a hydrogenetic ferromanganese crust dredged on "Haxby Seamount", one of the Marie Byrd seamounts on Antarctica's Pacific continental margin (69 °8.16'S, 123 °12.76'W-69 °8.53'S, 123 °13.13'W; water depth: 1502–1734 m,

Fig. 1)[16]. Hydrogenetic ferromanganese crusts precipitate slowly from seawater on hard substrates in areas with very low or absent sedimentation, making them reliable archives of past SO seawater compositions with minimal diagenetic alteration. Age control of ferromanganese crusts can be obtained using ^{230}Th and ^{10}Be dating methods. To address the challenges posed by their slow growth rates (a few millimetres per million years) and complex internal structures, we apply laser ablation coupled with multiple-collector inductively coupled plasma mass spectrometry (LA-MC-ICPMS)[17,18] and two-dimensional (2D) mapping techniques[19,20]. This combined novel
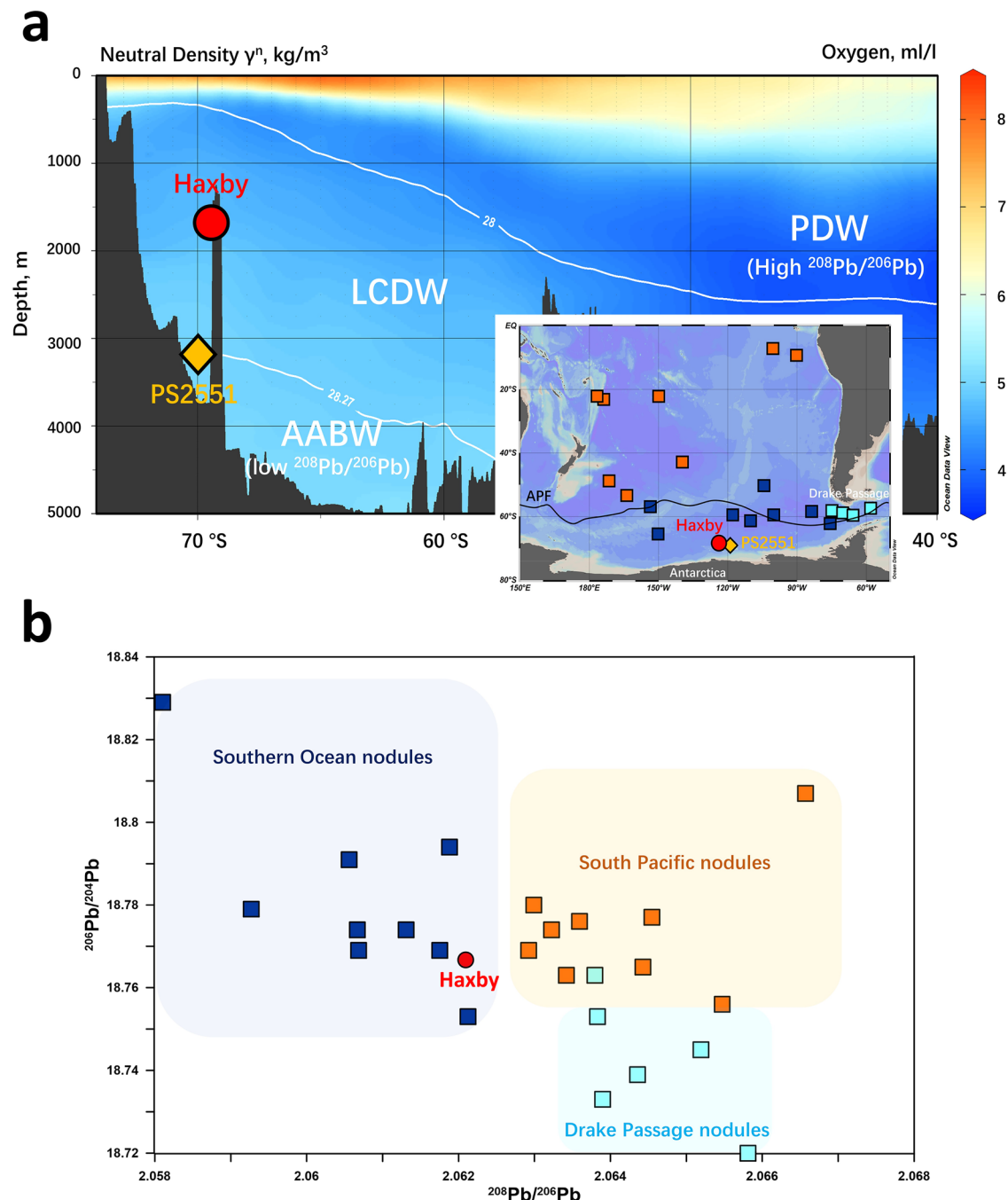

Fig. 1 | Sample locations. a Meridional distributions of oxygen levels (colour shading) overlain by neutral density (γⁿ) contours (white curves)[81,82]. Locations of ferromanganese crust Haxby and core PS2551 are shown by a red circle and a yellow diamond, respectively. Locations of ferromanganese nodules from the South Pacific (orange), Pacific sector of the SO (dark blue), and Drake Passage (light blue) are marked as squares in the inset map. **b** ^{208}Pb/^{206}Pb-^{206}Pb/^{204}Pb plot of preindustrial Pb isotope signals recovered from surfaces of ferromanganese nodules and crusts in the upper panel[30,40,83]. Southern Ocean nodules show that AABW in the Pacific sector is characterized by low ^{208}Pb/^{206}Pb (<2.0625) ratios, whereas South Pacific nodules show that Pacific waters, such as PDW, carry higher ^{208}Pb/^{206}Pb ratios (>2.0625). AABW Antarctic Bottom Water, PDW Pacific Deep Water, LCDW Lower Circumpolar Deep Water.

approach enables us to confidently resolve past Pb isotope variations on orbital timescales.

Lead has three radiogenic isotopes, i.e., ^{206}Pb, ^{207}Pb and ^{208}Pb produced from the decay of ^{238}U, ^{235}U and ^{232}Th, respectively, and one primordial isotope ^{204}Pb. Seawater Pb primarily originates from weathering of continental source materials supplied mainly via fluvial inputs[21,22] and, in polar regions, via glacial meltwaters. Due to its relatively short residence time in the ocean (~50 to 200 years)[23–25], Pb isotopes serve as sensitive tracers for continental inputs and basin-scale water mass mixing. In the SO, wind-driven upwelling transfers Circumpolar Deep Water (CDW), the main circum-Antarctic water mass, towards the surface south of the APF. In our study area, Lower CDW (LCDW) is mainly a mixture of AABW formed in the Ross Sea and North Atlantic Deep Water (NADW)[7,26], whereas less dense Pacific Deep Water (PDW) is entrained in Upper CDW (UCDW)[27] (Fig. 1a). At present, crust Haxby is located in the pathway of deep upwelling LCDW and thus ideally suited for monitoring deep water mixing in the high-latitude SO. Our data show marked changes in $^{208}Pb/^{206}Pb$ values across the MBE, which we attribute to shifts in the mixture between AABW and LCDW, highlighting the SO's role in regulating the global carbon cycle.

Results and discussion

Acquisition of orbital-resolution Pb isotopes time series

Previous methods[18] for acquiring orbital-scale seawater isotope records from ferromanganese crusts and nodules have been limited by issues such as age profile and proxy data measured along different laser tracks, as well as unidentifiable post-diagenetic effects, both of which introduce significant uncertainty into the time series records. In this study, we overcome these challenges by performing sequential 2D scans of elemental and isotopic compositions on the same area of the crust (detailed in Methods). This allows us to precisely extract elemental ratios, age data, and Pb isotope compositions from each pixel (Figs. 2 and 3). Furthermore, post-diagenetic material can be clearly identified and excluded, ensuring consistent, high-resolution Pb isotope records across different analyzed areas.

First, a scan of Mn/Fe ratios was conducted over a large area, which revealed two main growth patterns. The first is represented by a prominent laminated structure with alternating high and low Mn/Fe bands (Fig. 2a). The Mn/Fe ratios in this structure range from 1 to 2 and reflect a typical hydrogenetic growth pattern (Mn/Fe ratios of 0.5-2)[28]. The second pattern comprises discrete patches with Mn/Fe ratios below 0.5, which disrupt the laminations and suggest post-diagenetic process.

The age information based on the $^{230}Th_{ex}$ method (detailed in Methods) revealed average growth rates of each line scan in Figs. 2b and 2c ranging from 1.0 to 1.5 mm/Myr. These are within the typical range for hydrogenetic growth[29] and are consistent with the 1.7 mm/Myr growth rate derived from $^{10}Be/^9Be$ dating[30]. While ferromanganese crusts are generally assumed to grow at nearly constant rates over glacial-interglacial cycles, our $^{230}Th_{ex}$ results reveal episodic growth patterns alternating between extremely slow growth (0.3-0.6 mm/Ma) and fast growth with the fastest rate exceeding 10 mm/Myr (Supplementary Fig. 6). These fast growth episodes, which all occurred during glacial periods at average ages of ~22 ka, ~61 ka, ~189 ka, ~277 ka, ~359 ka, and ~439 ka, are associated with reduced flow velocity[31], nutrient enrichment[32] and oxygen depletion[33] in LCDW.

The rapid growth episodes fall into two distinct categories. The first and more common type retains the laminated Mn/Fe structure (Mn/Fe = 1-2) typical of hydrogenetic growth, and these intervals were used to extract the seawater Pb isotope records. While such fast growth rates exceed the common hydrogenetic range (<6 mm/Myr)[29], our results show that they can occur under specific environmental conditions without compromising their hydrogenetic origin. The second type, for example, observed at ~61 ka, displays Mn/Fe ratios below

0.5 and Pb/Tl ratios exceeding 15 (Fig. 3d). This indicates either mixed hydrothermal/hydrogenetic growth, characterized by lower Tl concentrations[28], and/or extensive post-depositional dissolution of Tl-bound Mn oxides under reductive glacial LCDW conditions[33]. Given these complexities, this section was excluded from the Pb isotope time series. Although fast-growing layers cover relatively large areas in the 2D scans, they represent only brief time intervals and therefore exert only limited influence on the overall Pb isotope record.

Subsequent laser scans for Tl and Pb isotopes were solely conducted in the section shown in Fig. 2b, in which the youngest surface is preserved. Age data and Pb isotope compositions from two separate laminated sections (sec-1 and sec-2 in Fig. 3) were processed separately, providing two independent Pb isotope time series. Consistent $^{206}Pb/^{204}Pb$ and $^{208}Pb/^{206}Pb$ records from these two areas (Supplementary Fig. 10) validate its reproducibility.

Controls of Pb isotope variations

The $^{208}Pb/^{206}Pb$ data show pronounced cyclic variations over the past 800 kyr, with generally lower $^{208}Pb/^{206}Pb$ during warm times than observed during cold periods (Fig. 4d). A key observation is that pre-MBE interglacials had systematically higher $^{208}Pb/^{206}Pb$ ratios than post-MBE interglacials. While variations in terrestrial Pb sources may have influenced these records[18], the evidence presented below strongly supports the conclusion that water mass mixing[34] has been the dominant control on Pb isotope signatures of the crust Haxby record.

Modern seawater survey and model simulations show that the distribution of Pb isotope compositions in the SO reflects water mass advection and mixing[35]. Similarly, spatial patterns of Pb isotope compositions recovered from Pleistocene sediments and surfaces of ferromanganese crusts/nodules in the Pacific sector of the SO also clearly show a closer alignment with water mass distributions than with shifts in terrestrial Pb sourcing[30]. In support of this, the Pb isotope time series in crust Haxby after 220 ka closely covaried with the authigenic Pb isotope record of sediment cores SO213-59-2 and SO213-60-1 located in the sub-Antarctic Pacific further north (Supplementary Fig. 10), which has been interpreted in terms of variable water masses contributions to LCDW over the past 220 ka[36]. This is also in line with records of other water mass tracers, such as radiogenic Nd isotopes and $\delta^{13}C$, from the same cores[36].

Given crust Haxby's proximity to the Antarctic continent, it is important to assess whether variable detrital Pb inputs may have influenced its isotopic compositions. While benthic fluxes are known to overprint seawater Pb and Nd isotope signatures in authigenic phases of some Antarctic continental margin sediments[15,37], such processes are minimized in crusts Haxby, which grew on hard substrates on a seamount, where sedimentation rates are known to be extremely low[36]. Moreover, it had been previously shown that at present boundary processes on the West Antarctic continental margin do not significantly change the Nd isotopic composition of bottom waters there[38]. Had detrital input from West Antarctica dominated the Pb isotope signals of crust Haxby, one would, for example, expect $^{208}Pb/^{206}Pb$ signatures of 2.044–2.056, which had been measured on near-coastal sediments from the Amundsen Sea embayment directly south of our sampling location[39]. These values are significantly lower than those recorded in crust Haxby (Fig. 4d), which displays more Pacific-sourced signals, consistent with upwelling of Pacific-derived deep waters in this region[30]. In contrast, sediment core SO213-60-1, located ~20° further north, actually recorded a more pronounced contribution of Antarctic Pb signatures, consistent with its greater depth and stronger influence by AABW. Furthermore, input from variable Antarctic sources has led to distinct Pb isotope distributions along the Antarctic margin. Moving from the western to the eastern Pacific sector of the SO and into Drake Passage, $^{208}Pb/^{206}Pb$ ratios systematically increase while $^{206}Pb/^{204}Pb$ ratios decrease in the surfaces
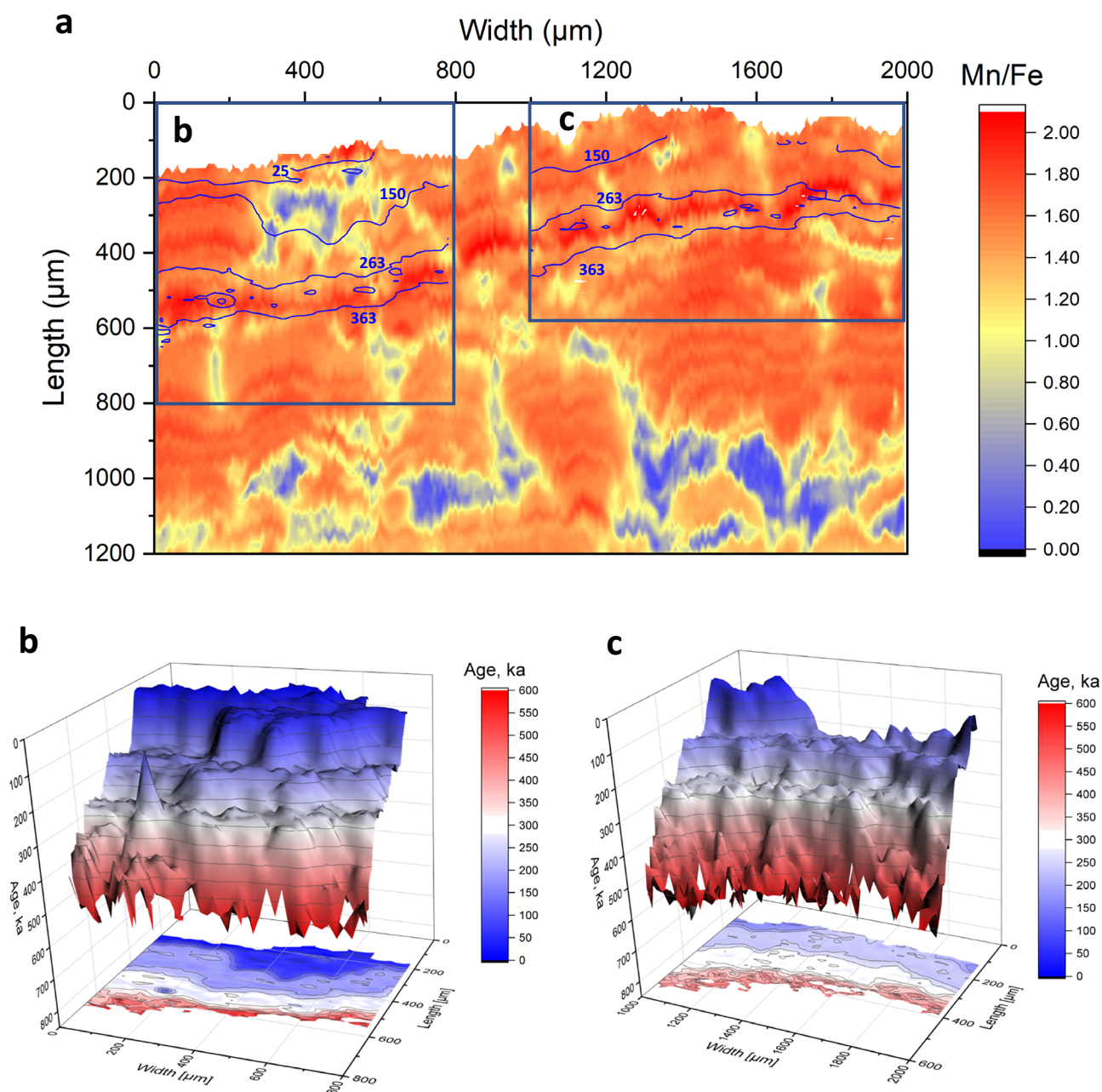
Fig. 2 | Mn/Fe composition and age of the studied ferromanganese crust. a Mn/Fe ratios with age contours marking glacial intervals (ages in ka). The glacial age contours always correspond to relatively low Mn/Fe ratios, while relatively high Mn/Fe ratios reflect interglacials. **b** and **c** show 2D/3D age images for the selected areas indicated in **a**.

of ferromanganese nodules/crusts (Figs. 1 and 5)[30,40]. In our record (Fig. 5), the interglacial Pb isotope signatures before and after the MBE show a clear shift in $^{208}Pb/^{206}Pb$, while the $^{206}Pb/^{204}Pb$ ratios essentially remained unchanged. This pattern is inconsistent with changes in inputs from Antarctic Pb sources. The absent shift in $^{206}Pb/^{204}Pb$ further rules out a primary control by "incongruent weathering", which would have produced and released a more radiogenic, higher $^{206}Pb/^{204}Pb$, signal in the weathering solutions than that of the source rocks as a consequence of preferential chemical weathering or radiation damage of fresh labile accessory silicate minerals, during the early phases of interglacial ice sheet retreat[18,41]. Nearby sediment cores such as PS2551 also show no significant change in clay mineralogy across the MBE, despite strong glacial-interglacial variability, further suggesting that the provenance of terrestrial material remained the same[42].

By contrast, Antarctic-sourced deep waters, such as AABW, exhibit a much lower $^{208}Pb/^{206}Pb$ signal than Pacific-sourced deep water, e.g., PDW, while these two water masses show a similar range of $^{206}Pb/^{204}Pb$ ratios (Fig. 5). Therefore, the variability in the $^{208}Pb/^{206}Pb$ record of crust Haxby is best explained by shifts in the relative contributions of AABW and PDW to LCDW. We conclude that the observed changes in $^{208}Pb/^{206}Pb$ are primarily driven by water mass mixing between these deep water sources.

Implications for SO circulation changes

Our record from crust Haxby documents higher glacial than interglacial $^{208}Pb/^{206}Pb$ ratios of LCDW. This suggests increased proportions of PDW relative to AABW in LCDW during glacials. More radiogenic Nd isotope signatures[43–45] and increased dissolved
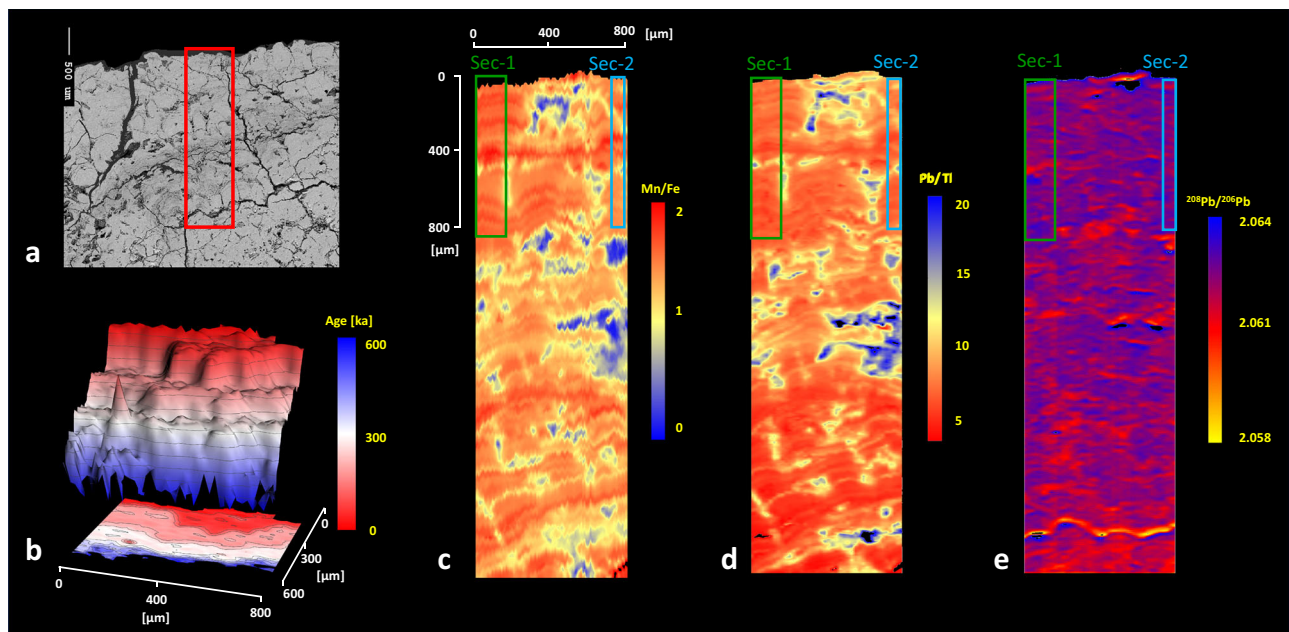
Fig. 3 | Elemental and isotope compositions of a selected area of crust Haxby.
a Backscatter Electron (BSE) image analysed by electron microprobe. The area marked by the red rectangle was used for Pb and Tl elemental as well as Pb isotope analyses; **b** 2D and 3D age images; **c** Mn/Fe ratios; **d** Pb/Tl ratios; and **e** $^{208}Pb/^{206}Pb$ ratios. The rectangles outlined in green and blue in **b**–**d** mark the laminated sections (Sec-1 and Sec-2) selected for the extraction of the high-resolution time series. The close consistency between Mn/Fe and Pb/Tl ratios indicate minimal spatial shifts between individual scan sections.

inorganic carbon (DIC) concentrations[46,47] in LCDW during glacial periods have provided evidence that PDW replaced shoaled NADW as a dominant component of LCDW[6,47]. Moreover, a larger gradient in Nd isotopic compositions between AABW and LCDW during the last glacial period[43] suggests reduced vertical mixing, likely due to a more stratified deep SO and weakened upwelling. This change would have led to less AABW being incorporated into LCDW. In addition, both modern data and paleorecords show that upper water column Pb isotope signals can be efficiently transferred to the deep ocean via sinking particles without changing water mass mixing[35,48–50]. However, biological productivity, represented by the Ba$_{bio}$ record from nearby site PS2551 (Fig. 4c)[42] and Ba$_{bio}$, biogenic opal and diatom concentrations at site PS58/254[51,52], was lower during glacials than during interglacials, suggesting that enhanced particle sinking was unlikely responsible for the higher $^{208}Pb/^{206}Pb$ ratios of glacial LCDW. Therefore, we attribute the elevated $^{208}Pb/^{206}Pb$ ratios in glacial LCDW to increased PDW subduction and a reduced upward supply of AABW.

Likewise, the higher $^{208}Pb/^{206}Pb$ ratios in LCDW during the lukewarm interglacials than during more recent interglacials suggest reduced mixing of AABW relative to PDW (Fig. 6). Unlike the shoaled and likely more sluggish Atlantic Meridional Overturning Circulation (AMOC) during recent glacial periods[53,54], evidence from Nd isotopes[10] and sediment grain size[55] records in the Atlantic Ocean suggests that AMOC geometry and strength were similar during lukewarm and recent interglacials. Compilation of global benthic foraminifera $\delta^{13}C$ data covering the last 800 ka shows little change, by inference, AMOC strength between pre- and post-MBE interglacials[56], which is consistent with a benthic foraminifera $\delta^{13}C$ record from one of the Marie Byrd Seamounts[57]. Furthermore, comparable Nd isotope compositions of LCDW during interglacials before and after the MBE indicate little increase in the mixing of PDW into LCDW during the lukewarm interglacials[58–61]. Taken together, the elevated $^{208}Pb/^{206}Pb$ ratios in LCDW primarily resulted from reduced admixture of AABW into LCDW, indicative of a more stratified deep SO, during lukewarm interglacials.

Several processes may have contributed to reduced SO deep water mixing during the lukewarm interglacials[11–13]. One potential

mechanism is the reduced dynamic range of SO overturning during these periods, as suggested by diminished productivity inferred from Ba/Fe ratios (Fig. 4b) from the Atlantic sector of the SO[11]. Similar reductions in productivity, indicated by Ba$_{bio}$ data, have also been observed at site PS2551 (Fig. 4c)[42]. However, productivity records across the SO as a whole and even within its individual ocean basins are not consistent. While some studies report elevated productivity during specific interglacials before the MBE[42,51], another study suggests little decline in productivity during lukewarm interglacials[57]. These discrepancies may reflect spatial variability in sea-ice cover or the positioning of SO fronts, yet the overall trend suggests that productivity during lukewarm interglacials was generally lower than during more recent interglacials. Another potentially important process is an increase in AABW density. Enhanced sea ice formation (Fig. 4e) and lower Antarctic air temperatures (Fig. 4g) during lukewarm interglacials could have facilitated AABW production and the formation of denser AABW[62,63]. This hypothesis is supported by the observed steeper latitudinal $\delta^{13}C$ gradient between northern- and southern-sourced waters in the equatorial Atlantic Ocean[8], as well as model simulations[12]. The resulting increased density contrast within the deep SO would have strengthened ocean stratification between mid- and deep-waters, limiting mixing between AABW and LCDW.

The stronger stratification of the deep SO during the lukewarm interglacials coupled with reduced upwelling and extended sea ice cover around Antarctica, would have diminished the exchange of carbon between the deep ocean and the atmosphere (Fig. 6). A box model study[64] suggests that the combination of these SO processes (i.e., increased sea ice coverage and enhanced deep ocean stratification) under presence of a strong NADW export[10] lowered atmospheric CO_2 levels by as much as 36 ppm. This finding helps to explain the observed CO_2 concentration difference of 30-40 ppm between lukewarm and post-MBE interglacials[2,65]. If deep ocean stratification diminishes[66] and sea ice production decreases[67] in response to anthropogenic warming in the future, our results may suggest a long-term future weakening of the SO's capacity to sequester carbon in the ocean interior.
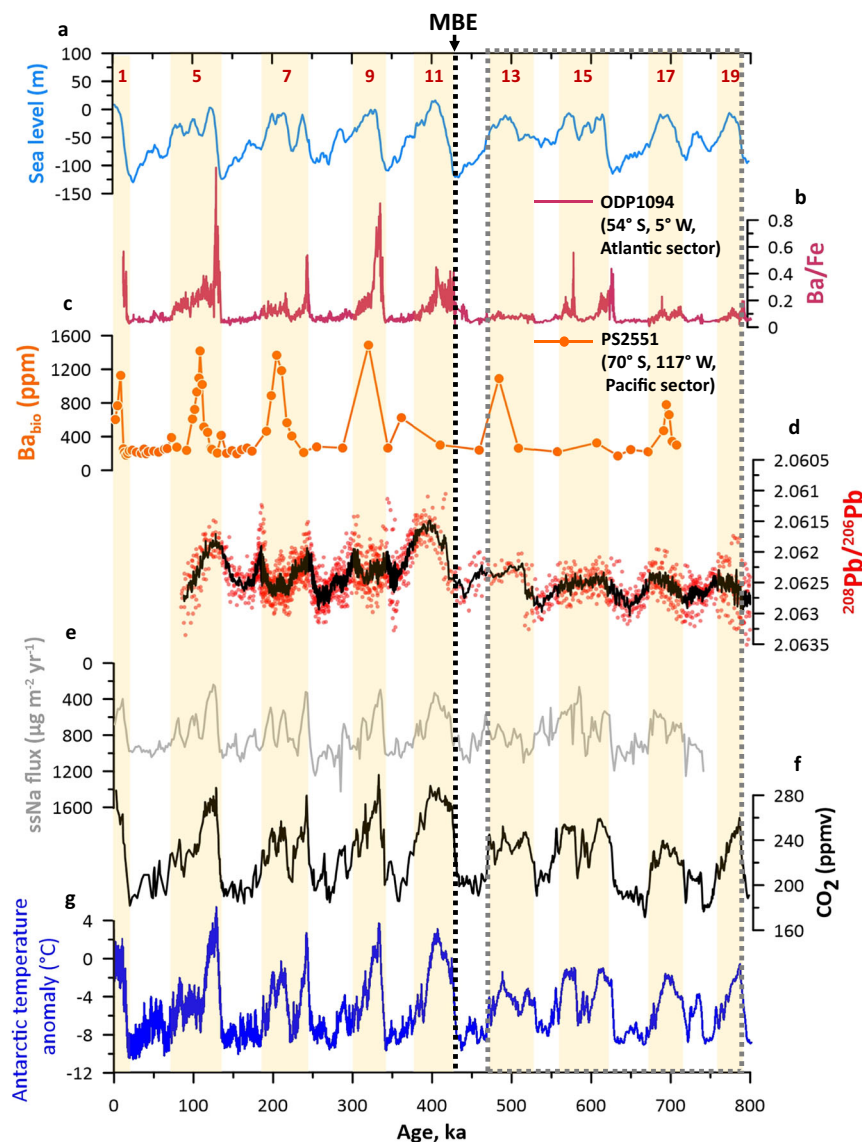
Fig. 4 | Compilation of paleoclimatic records during the past 800 ka. a Stack of sea level reconstructions[84]; **b** Ba/Fe ratio at ODP Site 1094[11]; **c** Ba$_{bio}$ at site PS2551[42]; **d** ^{208}Pb/^{206}Pb time series in sec-1, note that this record is shown inverted. The black line represents 5-point runing mean values; **e** sea salt Na (ssNa) flux, a proxy for sea ice extent[85]; **f** atmospheric CO_2[2]; **g** Antarctic air temperature anomaly[1]. The white and yellow vertical shadings denote glacial and interglacial periods, respectively, based on the standard marine isotope stage (MIS) classification from the LR04 benthic $\delta^{18}O$ stack[86]. Interglacial MISs are numbered at the top. The box with the grey dotted outline illustrates the time interval with lukewarm pre-MBE interglacial periods recorded in crust Haxby. MBE Mid-Brunhes Event.

Methods

Sample preparation

The surface of crust Haxby was initially coated with epoxy resin to preserve its structure before being cut into slabs suitable for laser ablation analysis. After each cut, the sample was re-embedded in epoxy resin to ensure continued protection of its natural structure. Ultimately, a slab approximately 5 cm long, 2 cm wide, and 0.3 cm thick was sectioned using a microtome saw. The exposed surface for LA-MC-ICP-MS analysis was then polished using Bühler "Micropolish" (Bühler GmbH, Duesseldorf, Germany). Following polishing, the sample surface was thoroughly cleaned with Milli-Q water to remove any potential contaminants.

Laser ablation analyses

Two-dimensional (2D) elemental and isotopic ratio maps were generated from selected areas of the sample. Prior to laser ablation, backscattered electron images were acquired using an electron microprobe. A target area of 2000 μm x 2775 μm (width x length) for

LA-MC-ICP-MS analyses is outlined by a red rectangle in Supplementary Fig. 1. These analyses were performed using a 193 nm Analyte Excite Excimer Laser Ablation System connected to a Thermo Scientific Neptune Plus MC-ICP-MS at GEOMAR Kiel. Three distinct measurements were conducted in sequence, each with specific instrumental settings:

1). Mn and Fe isotope analyses (Supplementary Fig. 2): Semi-quantitative overview images (10 μm spot size and 10 × 8 μm step size) were obtained to assess the overall Mn and Fe concentration variability and Mn/Fe ratios in the sample. This step was used to visualize the sample's growth structure and guide the selection of areas for more detailed analyses.

2). Th and U isotope analyses (Supplementary Figs. 3 and 4): Using a 25 μm spot size and 25×20 μm step size, measurements were taken to create age images in two selected areas: area-I (0-800 μm width, 0-1900 μm length, Fig. 2b) and area-II (1000-2000 μm width, 0-900 μm length, Fig. 2c).
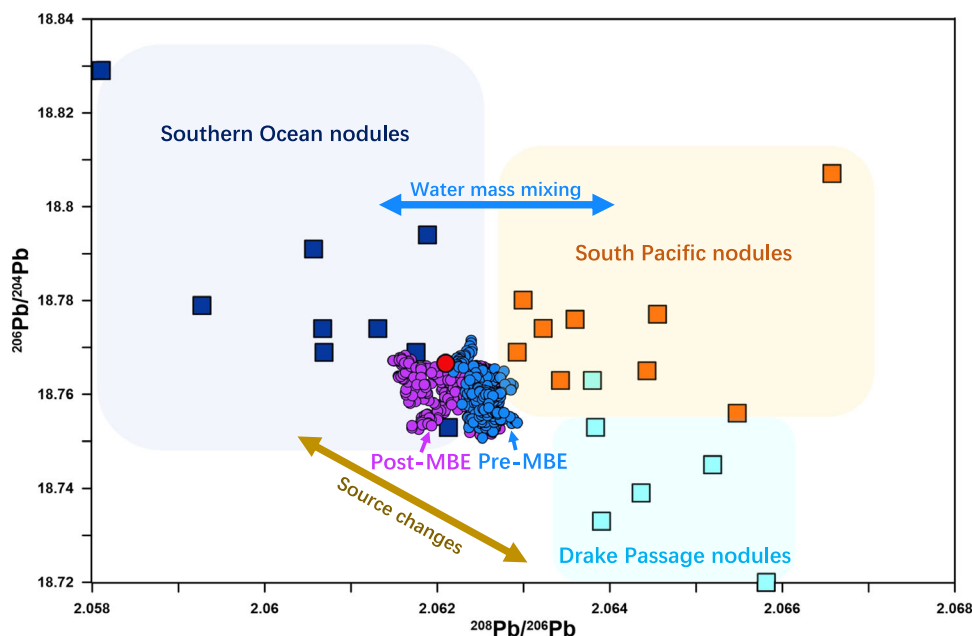
Fig. 5 | $^{208}Pb/^{206}Pb$ vs $^{206}Pb/^{204}Pb$ ratios. Pb isotope data of crust Haxby are shown by circles. The purple and blue circles mark 5-point running mean Pb isotope values during post- and pre-MBE interglacials, respectively. The red circle indicates the bulk composition analysed by the conventional approach[30]. Coloured squares denote Pb isotope data from discrete surface scrapings of ferromanganese nodules[40,83] shown in Fig. 1. These Pb isotope data from Southern Ocean and South Pacific nodules are used to reflect pre-industrial Pb isotope signals of southern- and north Pacific-sourced deep waters, respectively. MBE Mid-Brunhes Event.
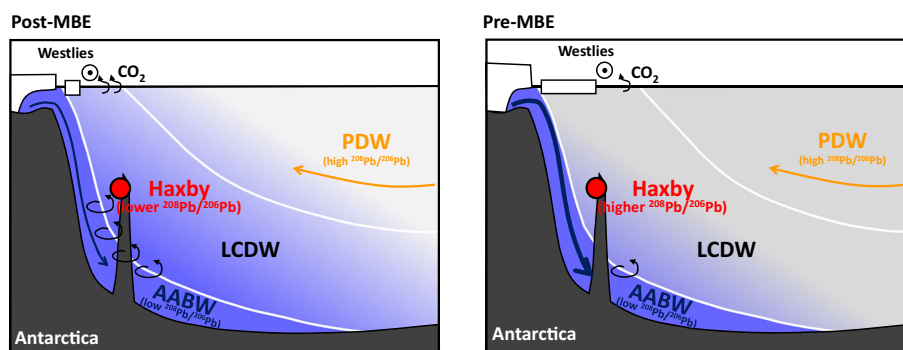
Fig. 6 | Schematic illustration of Southern Ocean circulation changes before and after the Mid-Brunhes Event (MBE). During pre-MBE interglacials, the deep Southern Ocean was more strongly stratified than in more recent interglacials, with reduced mixing of Antarctic Bottom Water (AABW), characterized by low $^{208}Pb/^{206}Pb$, into the Lower Circumpolar Deep Water (LCDW). This enhanced stratification, together with weaker upwelling and expanded sea-ice cover around Antarctica, would have limited CO_2 exchange between the deep ocean and the atmosphere. PDW Pacific Deep Water.

3). Pb and Tl isotope analyses (Supplementary Fig. 5): Using a 25 μm spot size and 25 × 20 μm step size, measurements were conducted to map Pb and Tl concentrations and generate $^{206}Pb/^{204}Pb$ and $^{208}Pb/^{206}Pb$ ratio images.

Previous work[68] has shown that plasma conditions strongly influence elemental fractionation and ionization efficiency during laser ablation. The Normalized Argon Index (NAI), introduced by Ref. 68, serves as a proxy for plasma temperature and ionization efficiency. To ensure consistent and optimal plasma conditions across different sessions, we carefully adjusted laser parameters, such as spot size, fluence, and scan speed, and MC-ICP-MS settings (see Supplementary Table 1) to achieve high and stable NAI values (≥1) for all measurement sessions. This ensured minimal mass-dependent fractionation and enhanced ionization efficiency for the elements analyzed.

Mn and Fe images

As Mn and Fe are the primary constituents of ferromanganese crusts, Mn and Fe measurements provide direct insights into the sample's growth patterns. The purpose of these overview scans was to evaluate the internal elemental variability and distribution of Mn and Fe within the selected area. No external standards were used for calibration during these scans. Signals for ^{55}Mn, ^{56}Fe, and ^{57}Fe were simultaneously collected on Faraday cups (Supplementary Table 2).

While ^{56}Fe is the most abundant stable isotope of iron (91.75%), its signal overlaps with the strong signal from the $^{40}Ar^{16}O$ cluster in the gas blank. In contrast, ^{57}Fe, though free from major argon-derived interference, has a lower signal intensity due to its low abundance (2.11%). The interferences for all isotopes were corrected based on gas blank data collected prior to each line ablation. Despite these different interferences in the gas blank during analysis, the consistent intensity patterns between ^{56}Fe and ^{57}Fe (Supplementary Fig. 2a and S2b) suggest both provide reliable information towards the internal Fe distribution. On the other hand, Mn measurements are more straightforward since ^{55}Mn, the only stable isotope of Mn, is free from major argon interferences. We normalized the ^{55}Mn intensity to the combined ^{56}Fe and ^{57}Fe ion intensities to indicate the Mn/Fe variability (Supplementary Fig. 2d) and derive the Mn/Fe ratio (Fig. 2a) based on

their isotope abundances. No smoothing of data points was applied in the Mn/Fe image.

Th and U images

Following the Mn and Fe overview scans, Th and U isotope images were generated. For correction, line measurements of the NIST-SRM610, USGS NOD-A-1, and USGS NOD-P-1 standards were taken after each set of sample lines. The USGS NOD-A-1 and USGS NOD-P-1 standards, which consist of ferromanganese nodule powders, were pressed into pellets without chemical binders.

Two scan profiles were carried out to investigate the use of the $^{230}Th_{ex}/^{232}Th$ and $^{234}U_{ex}/^{238}U$ as chronology tools. The first scan collected ^{230}Th, ^{232}Th and ^{238}U signals with ^{232}Th and ^{238}U on Faraday cups and ^{230}Th on an ion counter. The second scan measured ^{232}Th and ^{238}U on Faraday cups and ^{234}U on the ion counter (Supplementary Table 2). Two areas (I in Supplementary Fig. 3 and II in Supplementary Fig. 4), covering nearly the entire Mn/Fe image surface, were scanned twice to capture paired Th and U isotope measurements.

The raw data were background-corrected based on gas blank measurements collected before each line ablation. To enhance image quality, data smoothing was applied once. For each individual pixel, the value was averaged with a weighted combination of its neighbouring data points: the once-weighted values from the four diagonal neighbours, the three-times weighted values from the two nearest horizontal and two nearest vertical neighbours, and the seven-times weighted value from the central pixel.

As shown Supplementary Figs. 3a and 4a, ^{230}Th signals decrease with increasing depth in the sample profiles and eventually reach secular equilibrium. However, there is no decreasing trend in ^{234}U signals with increasing depth in the sample profiles. Early studies showed that $^{234}U_{ex}/^{238}U$ profiles generally give higher growth rates than those derived from $^{230}Th_{ex}/^{232}Th$ data profiles[69,70] because of the higher diffusivity of U in the ferromanganese crusts[71,72]. Our results also suggest that ferromanganese crusts are not a closed system for U, ruling out $^{234}U_{ex}/^{238}U$ as a reliable chronology tool for dating this crust. In addition, ^{230}Th concentrations in the topmost surface part in area-I are systematically higher than in area II (Supplementary Figs. 3a and 4a), indicating the topmost surface materials in area-II have been lost during recovery of the sample. The following laser ablation analyses thus only focused on the area-I.

Pb and Tl images

Prior to measurements of Pb and Tl isotopes, the sample surface was pre-ablated by triple laser pulses with $3\,J\,cm^{-2}$ laser power density in order to eliminate potential surface contamination. Image data for Pb and Tl have been run with the line measurements of NIST-SRM610, USGS NOD-A-1 and USGS NOD-P-1 standards before and after every set of sample lines to monitor drift control and to obtain a reliable normalization of instrumental mass fractionation. The signals of ^{202}Hg, ^{203}Tl, ^{204}Pb, ^{205}Tl, ^{206}Pb, ^{207}Pb, ^{208}Pb were collected by Faraday cups (Supplementary Table 2). The ^{202}Hg signal was specifically monitored to correct for isobaric interference of ^{204}Hg on ^{204}Pb. Because the $^{202}Hg/^{204}Hg$ ratio can vary between measurement sessions, we applied an optimized $^{202}Hg/^{204}Hg$ value based on our recent calibration method[30], rather than using a fixed literature value. After the blank correction for the gas blank data collected before each line ablation, the signal intensity images of ^{208}Pb and ^{205}Tl are shown in Supplementary Fig. 5a and 5b. Due to the similarity of Pb and Tl isotope variations, we only show the intensity images of the most abundant isotopes, ^{208}Pb and ^{205}Tl. The intensity ratio of $^{208}Pb/^{205}Tl$ is used to indicate Pb/Tl variations, and the Pb/Tl ratios are derived based on their isotope abundances, as shown in Fig. 2. To improve the image quality via data smoothing, individual pixel intensities were averaged twice with neighbouring data points for both Pb and Tl.

Our method applied for the normalisation of instrumental mass fractionation of Pb isotope is based on the assumption that the fractionation factors during measurements of samples and the selected standards are identical when the plasma conditions of MC-ICP-MS are consistent for all measurements[68]. The plasma states of analyses for samples and standards were tuned to NAI values of about 1[68]. These NIST-SRM610, USGS NOD-A-1 and USGS NOD-P-1 standards cover a wide $^{206}Pb/^{204}Pb$ and $^{208}Pb/^{206}Pb$ range with different matrix compositions. The combination of these three different standards thus provides the best approach to maximize accuracy and precision of the measurements covering similar Pb isotope signal intensities and considering matrix composition variations. The Pb isotope fractionation factor was obtained from the optimal values of these three standards using the linear regression normalization method[73]. The details of this method are described in a recent paper[30]. The final images for $^{208}Pb/^{206}Pb$ and $^{208}Pb/^{206}Pb$ are shown in Supplementary Fig. 5c and Fig. 3e. Six repeat analyses of these the reference materials (three analyses before and three analyses after analytical sessions) yielded the following ratios and uncertainties: $^{206}Pb/^{204}Pb = 17.052 \pm 0.003$ and $^{208}Pb/^{206}Pb = 2.1695 \pm 0.0005$ for NIST SRM 610, $^{206}Pb/^{204}Pb = 18.935 \pm 0.013$ and $^{208}Pb/^{206}Pb = 2.0555 \pm 0.0023$ for USGS NOD-A-1, and $^{206}Pb/^{204}Pb = 18.689 \pm 0.019$ and $^{208}Pb/^{206}Pb = 2.0681 \pm 0.0010$ for USGS NOD-P-1 (all uncertainties are provided as 2 SD (n = 2640)). The good agreement between the double spike solution data[74] and the LA-MC-ICPMS data show that our measurements are reliable. NIST SRM 610, which has Pb and Hg concentrations similar to those of the Haxby crust, was used as the principal standard to assess measurement precision[30].

Age model

The U/Th images reflect the temporally variable Th concentrations in the crust. The ^{230}Th data are normalized to ^{232}Th to obtain the variability of the ^{230}Th flux. As shown in Supplementary Figs. 3 and 4, ^{234}U and ^{238}U covary, and $^{234}U/^{238}U$ is well diffused in the scanned area. The excess ^{230}Th ($^{230}Th_{ex}$), unsupported by ^{234}U decay, of each data point is thus calculated as:

$$\left[{}^{230}Th_{ex}/{}^{232}Th \right] = \left[{}^{230}Th/{}^{232}Th \right] - \beta \times \left[{}^{238}U/{}^{232}Th \right] \qquad (1)$$

The β is the combined factor for the yield of ion counter, instrumental Th isotope fractionation, $^{238}U/^{232}Th$ fractionation and $^{234}U/^{238}U$ ratio. The $[^{230}Th_{ex}/^{232}Th]$ value is expected to reach secular equilibrium after about seven half-lives of ^{230}Th. A value of 1500 for β was derived as it leads to $[^{230}Th_{ex}/^{232}Th]$ values in the old layers approaching zero (i.e., secular equilibrium of $^{230}Th/^{234}U$). Because no trend of ^{234}U concentration decrease compared to ^{238}U concentrations was observed and the influence of ^{234}U decay is overall small, its variability as a function of time has not been considered.

The age of each data point can be calculated:

$$Age = \ln\left(\left[{}^{230}Th_{ex}/{}^{232}Th \right]_0 / \left[{}^{230}Th_{ex}/{}^{232}Th \right] \right) / \ln(2) \times T_{1/2} \qquad (2)$$

The half-life ($T_{1/2}$) of ^{230}Th is 75690 yrs. The initial Th isotope ratio $[^{230}Th_{ex}/^{232}Th]_0$ of 35000 (counts/V) is obtained from the highest measured values in the scanned surface area. The age distribution images are shown in Fig. 2 of the main manuscript, and the corresponding variations in incremental growth rate are presented in Supplementary Fig. 6.

Our results show that the initial $^{230}Th_{ex}/^{232}Th$ ratio was slightly variable. For instance, the outer, stratigraphically "younger" layer on the age plateaus of 189 ka and 277 ka shows slightly older "apparent" ages (Supplementary Fig. 7). This seemingly paradoxical observation, in our opinion, has to be taken as an indication, that certain

assumptions in the $^{230}Th_{ex}$ dating method have come to a limit. One of those assumptions is a constant initial $^{230}Th_{ex}/^{232}Th$ ratio, applicable for the entire crust. However, both the $^{230}Th_{ex}$ and the ^{232}Th concentration can change through time (e.g., due to changing lateral transport by different water masses). This finding is supported by the variable initial $^{230}Th_{ex}/^{232}Th$ ratios found in deep-sea corals from nearby locations[75]. The changes of initial $^{230}Th_{ex}/^{232}Th$ ratios are likely related to water mass changes, because the declined initial $^{230}Th_{ex}/^{232}Th$ ratios (indicated by reversed ages) generally coincide with low $^{208}Pb/^{206}Pb$ ratios (Supplementary Fig. 7b). The influence of the initial $^{230}Th_{ex}/^{232}Th$ ratio variability on calculated ages is less prominent during the slow-growing episodes, so only the ages during these periods are used to date the crust (as shown in Supplementary Fig. 7). Due to the significant age uncertainty caused by variable initial $^{230}Th_{ex}/^{232}Th$ ratios, our age model is not reliable for resolving high temporal resolution variations, such as sub-orbital or millennial scale changes. As a result, we focused our analysis on changes occurring on glacial-interglacial timescales.

The dating method based on the $^{230}Th_{ex}$ approach enables us to construct an age model extending back to approximately 450 ka (5-6 half-lives of ^{230}Th). For deeper layers, ages are inferred from Pb/Tl variations. In hydrogenetic ferromanganese crusts, Tl is mainly bonded to vernadite (δ-MnO_2), the most abundant mineral phase, whereas Pb has a high affinity with the amorphous FeO-OH phase[76]. Therefore, the Pb/Tl ratio shows a negative correlation with Mn/Fe, which is supported by the high consistency between Pb/Tl and Mn/Fe ratios in crust Haxby (Fig. 3 and Supplementary Fig. 7a). The data after 450 ka clearly show systematic variations between high Pb/Tl (low Mn/Fe) during glacial times and low Pb/Tl (high Mn/Fe) during interglacial times (Supplementary Figs. 8 and 9). These variations may be related to changes in oxygen concentration in LCDW[33,77–79]. Consequently, we derived the ages between ~800 and 450 ka by tuning the Pb/Tl ratios to the Antarctic temperature record (Supplementary Figs. 8 and 9). Tie points were primarily placed at intervals of declining Pb/Tl values, which correspond to glacial periods in the Antarctic temperature record.

Data reproducibility for Pb isotope time series

The time series of Mn/Fe, Pb/Tl, $^{206}Pb/^{204}Pb$ and $^{208}Pb/^{206}Pb$ from two different laminated sections (sec-1 and sec-2 in Fig. 3) are presented in Supplementary Fig. 7 to assess the data reproducibility. Due to the influence of epoxy interference in the very surface part (topmost 25 μm as shown in the Supplementary Fig. 7b), the $^{208}Pb/^{206}Pb$ in this part cannot be well normalised and is thus excluded in the time series record. The Pb isotope data from porous areas (intensities of $^{208}Pb < 0.4$ V) are also excluded.

Manganese concentrations in ferromanganese crusts are sensitive to changes in redox conditions and serve as a redox proxy[80]. Although a general qualitative relationship exists between redox elements in crust Haxby and deep-ocean redox conditions, the interpretation of specific elemental ratios, such as Mn/Fe needs to be considered with caution. As illustrated in Supplementary Fig. 10b, the Mn/Fe time series records are inconsistent both along different lines in the same section and between different sections.

In contrast, the time series of $^{206}Pb/^{204}Pb$ and $^{208}Pb/^{206}Pb$ are consistent along the different analysis sections (Supplementary Fig. 10d and 10e). The overall $^{206}Pb/^{204}Pb$ and $^{208}Pb/^{206}Pb$ data extracted via laser ablation align well with the bulk Pb isotope compositions measured by conventional methods[30]. Moreover, the laser ablation $^{206}Pb/^{204}Pb$ and $^{208}Pb/^{206}Pb$ data from ~220 to 70 ka covary with authigenic Pb isotope data from the sediment cores recovered at sites SO213-59-2 and SO213-60-1 further north in the sub-Antarctic Pacific sector[36], further validating the reliability of the Pb isotope time series obtained by the LA-MC-ICPMS technique.

Data availability

All analytical data are available as open access in electronic form at the Zenodo data repository (https://doi.org/10.5281/zenodo.16907921; link: https://zenodo.org/records/16907921).

References

1. Jouzel, J. et al. Orbital and Millennial Antarctic climate variability over the past 800,000 years. *Science* **317**, 793–796 (2007).
2. Lüthi, D. et al. High-resolution carbon dioxide concentration record 650,000–800,000 years before present. *Nature* **453**, 379 (2008).
3. Jansen, J. H. F., Kuijpers, A. & Troelstra, S. R. A mid-Brunhes climatic event: long-term changes in global atmosphere and ocean circulation. *Science* **232**, 619–622 (1986).
4. Yin, Q. Z. & Berger, A. Insolation and CO_2 contribution to the interglacial climate before and after the Mid-Brunhes Event. *Nat. Geosci.* **3**, 243–246 (2010).
5. Marshall, J. & Speer, K. Closure of the meridional overturning circulation through Southern Ocean upwelling. *Nat. Geosci.* **5**, 171–180 (2012).
6. Sikes, E. L. et al. Southern Ocean glacial conditions and their influence on deglacial events. *Nat. Rev. Earth Environ*. 454–470, (2023).
7. Purkey, S. G. et al. A synoptic view of the ventilation and circulation of Antarctic bottom water from chlorofluorocarbons and natural tracers. *Annu. Rev. Mar. Sci.* **10**, 503–527 (2018).
8. Barth, A. M., Clark, P. U., Bill, N. S., He, F. & Pisias, N. G. Climate evolution across the Mid-Brunhes Transition. *Clim. Past* **14**, 2071–2087 (2018).
9. Bouttes, N., Swingedouw, D., Roche, D. M., Sanchez-Goni, M. F. & Crosta, X.Response of the carbon cycle in an intermediate complexity model to the different climate configurations of the last nine interglacials.*Clim, Past* **14**, 239–253 (2018).
10. Howe, J. N. W. & Piotrowski, A. M. Atlantic deep water provenance decoupled from atmospheric CO2 concentration during the lukewarm interglacials. *Nat. Commun.* **8**, 2003 (2017).
11. Jaccard, S. L. et al. Two modes of change in Southern Ocean productivity over the past million years. *Science* **339**, 1419–1423 (2013).
12. Yin, Q. Insolation-induced mid-Brunhes transition in Southern Ocean ventilation and deep-ocean temperature. *Nature* **494**, 222–225 (2013).
13. Kemp, A. E. S., Grigorov, I., Pearce, R. B. & Naveira Garabato, A. C. Migration of the Antarctic Polar Front through the mid-Pleistocene transition: evidence and climatic implications. *Quat. Sci. Rev.* **29**, 1993–2009 (2010).
14. Creac'h, L. et al. Unradiogenic reactive phase controls the εNd of authigenic phosphates in East Antarctic margin sediment. *Geochim. Cosmochim. Acta* **344**, 190–206 (2023).
15. Huang, H., Gutjahr, M., Kuhn, G., Hathorne, E. C. & Eisenhauer, A. Efficient extraction of past seawater Pb and Nd isotope signatures from Southern Ocean Sediments. *Geochem., Geophys. Geosyst.* **22**, e2020GC009287 (2021).
16. Gohl, K. The expedition of the Research Vessel "Polarstern" to the Amundsen Sea, Antarctica, in 2010 (ANT-XXVI/3). *Ber. zur. Polar-Meeresforsch. (Rep. Polar Mar. Res.), Bremerhav. Alfred Wegener Inst. Polar Mar. Res.* **617**, 173 (2010).
17. Christensen, J. N., Halliday, A. N., Godfrey, L. V., Hein, J. R. & Rea, D. K. Climate and Ocean Dynamics and the Lead Isotopic Records in Pacific Ferromanganese Crusts. *Science* **277**, 913–918 (1997).
18. Foster, G. L. & Vance, D. Negligible glacial–interglacial variation in continental chemical weathering rates. *Nature* **444**, 918–921 (2006).
19. Fietzke, J. et al. Century-scale trends and seasonality in pH and temperature for shallow zones of the Bering Sea. *Proc. Natl. Acad. Sci.* **112**, 2960–2965 (2015).

20. Fietzke, J. & Wall, M. Distinct fine-scale variations in calcification control revealed by high-resolution 2D boron laser images in the cold-water coral Lophelia pertusa. *Sci. Adv.* **8**, eabj4172 (2022).

21. Chen, M. et al. Boundary exchange completes the marine Pb cycle jigsaw. *Proc. Natl. Acad. Sci.* **120**, e2213163120 (2023).

22. Frank, M. Radiogenic isotopes: Tracers of past ocean circulation and erosional input. *Rev. Geophys.* **40**, 1001 (2002).

23. Cochran, J. K. et al. 210Pb scavenging in the North Atlantic and North Pacific Oceans. *Earth Planet. Sci. Lett.* **97**, 332–352 (1990).

24. Henderson, G. M. & Maier-Reimer, E. Advection and removal of 210Pb and stable Pb isotopes in the oceans: a general circulation model study. *Geochim. Cosmochim. Acta* **66**, 257–272 (2002).

25. Schaule, B. K. & Patterson, C. C. Lead concentrations in the north-east Pacific: evidence for global anthropogenic perturbations. *Earth Planet. Sci. Lett.* **54**, 97–116 (1981).

26. Solodoch, A. et al. How does Antarctic bottom water cross the Southern Ocean?. *Geophys. Res. Lett.* **49**, e2021GL097211 (2022).

27. Talley, L. D. Closure of the global overturning circulation through the Indian, Pacific, and Southern Oceans: Schematics and Transports. *Oceanography* **26**, 80–97 (2013).

28. Rehkämper, M. et al. Thallium isotope variations in seawater and hydrogenetic, diagenetic, and hydrothermal ferromanganese deposits. *Earth Planet. Sci. Lett.* **197**, 65–81 (2002).

29. Koschinsky, A. & Hein, J. R. Uptake of elements from seawater by ferromanganese crusts: solid-phase associations and seawater speciation. *Mar. Geol.* **198**, 331–351 (2003).

30. Huang, H. et al. Seawater Lead Isotopes Record Early Miocene to Modern Circulation Dynamics in the Pacific Sector of the Southern Ocean. *Paleoceanogr. Paleoclimatol.* **39**, e2024PA004922 (2024).

31. Lamy, F. et al. Five million years of Antarctic Circumpolar Current strength variability. *Nature* **627**, 789–796 (2024).

32. McCave, I. N., Carter, L. & Hall, I. R. Glacial-interglacial changes in water mass structure and flow in the SW Pacific Ocean. *Quat. Sci. Rev.* **27**, 1886–1908 (2008).

33. Jaccard, S. L., Galbraith, E. D., Martínez-García, A. & Anderson, R. F. Covariation of deep Southern Ocean oxygenation and atmospheric CO2 through the last ice age. *Nature* **530**, 207–210 (2016).

34. Frank, M., Whiteley, N., Kasten, S., Hein, J. R. & O'Nions, K. North Atlantic Deep Water export to the Southern Ocean over the past 14 Myr: Evidence from Nd and Pb isotopes in ferromanganese crusts. *Paleoceanography* **17**, 1022 (2002).

35. Olivelli, A. et al. Vertical transport of anthropogenic lead by reversible scavenging in the South Atlantic Ocean. *Earth Planet. Sci. Lett.* **646**, 118980 (2024).

36. Molina-Kescher, M. et al. Reduced admixture of North Atlantic Deep Water to the deep central South Pacific during the last two glacial periods. *Paleoceanography* **31**, 651–668 (2016).

37. Hallmaier, M. et al. Glacial Southern Ocean deep water Nd isotopic composition dominated by benthic modification. *Sci. Rep.* **15**, 2586 (2025).

38. Wang, R. et al. Boundary processes and neodymium cycling along the Pacific margin of West Antarctica. *Geochim. Cosmochim. Acta* **327**, 1–20, https://doi.org/10.1016/j.gca.2022.04.012 (2022).

39. Carlson, A. E., Beard, B. L., Hatfield, R. G. & Laffin, M. Absence of West Antarctic-sourced silt at ODP Site 1096 in the Bellingshausen Sea during the last interglaciation: Support for West Antarctic ice-sheet deglaciation. *Quat. Sci. Rev.* **261**, 106939 (2021).

40. Abouchami, W. & Goldstein, S. L. A lead isotopic study of circum-antarctic manganese nodules. *Geochim. Cosmochim. Acta* **59**, 1809–1820 (1995).

41. Gutjahr, M., Frank, M., Halliday, A. N. & Keigwin, L. D. Retreat of the Laurentide ice sheet tracked by the isotopic composition of Pb in western North Atlantic seawater during termination 1. *Earth Planet. Sci. Lett.* **286**, 546–555 (2009).

42. Hillenbrand, C.-D., Fütterer, D. K., Grobe, H. & Frederichs, T. No evidence for a Pleistocene collapse of the West Antarctic Ice Sheet from continental margin sediments recovered in the Amundsen Sea. *Geo-Mar. Lett.* **22**, 51–59 (2002).

43. Basak, C. et al. Breakup of last glacial deep stratification in the South Pacific. *Science* **359**, 900–904 (2018).

44. Hu, R. et al. Neodymium isotopic evidence for linked changes in Southeast Atlantic and Southwest Pacific circulation over the last 200 kyr. *Earth Planet. Sci. Lett.* **455**, 106–114 (2016).

45. Noble, T. L., Piotrowski, A. M. & McCave, I. N. Neodymium isotopic composition of intermediate and deep waters in the glacial south-west Pacific. *Earth Planet. Sci. Lett.* **384**, 27–36 (2013).

46. Ullermann, J. et al. Pacific-Atlantic Circumpolar Deep Water coupling during the last 500 ka. *Paleoceanography* **31**, 639–650 (2016).

47. Yu, J. et al. Last glacial atmospheric CO_2 decline due to widespread Pacific deep-water expansion. *Nat. Geosci.* **13**, 628–633 (2020).

48. Lanning, N. T. et al. Isotopes illustrate vertical transport of anthropogenic Pb by reversible scavenging within Pacific Ocean particle veils. *Proc. Natl. Acad. Sci.* **120**, e2219688120 (2023).

49. Huang, H., Gutjahr, M., Eisenhauer, A. & Kuhn, G. No detectable Weddell Sea Antarctic Bottom Water export during the Last and Penultimate Glacial Maximum. *Nat. Commun.* **11**, 424 (2020).

50. Wu, J., Rember, R., Jin, M., Boyle, E. A. & Flegal, A. R. Isotopic evidence for the source of lead in the North Pacific abyssal water. *Geochim. Cosmochim. Acta* **74**, 4629–4638 (2010).

51. Hillenbrand, C. D., Kuhn, G. & Frederichs, T. Record of a Mid-Pleistocene depositional anomaly in West Antarctic continental margin sediments: an indicator for ice-sheet collapse?. *Quat. Sci. Rev.* **28**, 1147–1159 (2009).

52. Konfirst, M. A., Scherer, R. P., Hillenbrand, C.-D. & Kuhn, G. A marine diatom record from the Amundsen Sea - Insights into oceanographic and climatic response to the Mid-Pleistocene Transition in the West Antarctic sector of the Southern Ocean. *Mar. Micropaleontol.* **92-93**, 40–51 (2012).

53. Curry, W. B. & Oppo, D. W. Glacial water mass geometry and the distribution of δ13C of ΣCO2 in the western Atlantic Ocean. *Paleoceanography* **20**, https://doi.org/10.1029/2004PA001021 (2005).

54. McManus, J. F., Francois, R., Gherardi, J. M., Keigwin, L. D. & Brown-Leger, S. Collapse and rapid resumption of Atlantic meridional circulation linked to deglacial climate changes. *Nature* **428**, 834–837 (2004).

55. Kleiven, H. F., Hall, I. R., McCave, I. N., Knorr, G. & Jansen, E. Coupled deep-water flow and climate variability in the middle Pleistocene North Atlantic. *Geology* **39**, 343–346 (2011).

56. Bouttes, N. et al. Carbon 13 Isotopes reveal limited ocean circulation changes between interglacials of the last 800 ka. *Paleoceanogr. Paleoclimatol.* **35**, e2019PA003776 (2020).

57. Williams, T. J. et al. Paleocirculation and ventilation history of Southern Ocean Sourced deep water masses during the last 800,000 years. *Paleoceanogr. Paleoclimatol.* **34**, 833–852 (2019).

58. Dausmann, V., Frank, M., Gutjahr, M. & Rickli, J. Glacial reduction of AMOC strength and long-term transition in weathering inputs into the Southern Ocean since the mid-Miocene: Evidence from radiogenic Nd and Hf isotopes. *Paleoceanography* **32**, 265–283 (2017).

59. Pena, L. D. & Goldstein, S. L. Thermohaline circulation crisis and impacts during the mid-Pleistocene transition. *Science* **345**, 318–322 (2014).

60. Tachikawa, K. et al. Eastern Atlantic deep-water circulation and carbon storage inferred from neodymium and carbon isotopic compositions over the past 1.1 million years. *Quat. Sci. Rev.* **252**, 106752 (2021).

61. Williams, T. J. et al. The role of ocean circulation and regolith removal in triggering the Mid-Pleistocene Transition: Insights from authigenic Nd isotopes. *Quat. Sci. Rev.* **345**, 109055 (2024).

62. Gunn, K. L., Rintoul, S. R., England, M. H. & Bowen, M. M. Recent reduced abyssal overturning and ventilation in the Australian Antarctic Basin. *Nat. Clim. Change* **13**, 537–544 (2023).

63. van Wijk, E. M. & Rintoul, S. R. Freshening drives contraction of Antarctic Bottom Water in the Australian Antarctic Basin. *Geophys. Res. Lett.* **41**, 1657–1664 (2014).

64. Hain, M. P., Sigman, D. M. & Haug, G. H. Carbon dioxide effects of Antarctic stratification, North Atlantic Intermediate Water formation, and subantarctic nutrient drawdown during the last ice age: Diagnosis and synthesis in a geochemical box model. *Glob. Biogeochem. Cycles* **24**, https://doi.org/10.1029/2010GB003790 (2010).

65. Bereiter, B. et al. Revision of the EPICA Dome C CO2 record from 800 to 600 kyr before present. *Geophys. Res. Lett.* **42**, 542–549 (2015).

66. Zhang, H. J., Whalen, C. B., Kumar, N. & Purkey, S. G. Decreased Stratification in the Abyssal Southwest Pacific Basin and Implications for the Energy Budget. *Geophys. Res. Lett.* **48**, e2021GL094322 (2021).

67. Raphael, M. N. & Handcock, M. S. A new record minimum for Antarctic sea ice. *Nat. Rev. Earth Environ.* **3**, 215–216 (2022).

68. Fietzke, J. & Frische, M. Experimental evaluation of elemental behavior during LA-ICP-MS: influences of plasma conditions and limits of plasma robustness. *J. Anal. Spectrom.* **31**, 234–244 (2016).

69. Chabaux, F., Cohen, A. S., Onions, R. K. & Hein, J. R. 238U-234U-230Th chronometry of Fe-Mn crusts: Growth processes and recovery of thorium isotopic ratios of seawater. *Geochim. Cosmochim. Acta* **59**, 633–638 (1995).

70. Chabaux, F., Unions, R. K., Cohen, A. S. & Hein, J. R. 238U234U230Th disequilibrium in hydrogenous oceanic FeMn crusts: Palaeoceanographic record or diagenetic alteration?. *Geochim. Cosmochim. Acta* **61**, 3619–3632 (1997).

71. Claude, C., Suhr, G., Hofmann, A. W. & Koschinsky, A. U-Th chronology and paleoceanographic record in a Fe-Mn crust from the NE Atlantic over the last 700 ka. *Geochim. Cosmochim. Acta* **69**, 4845–4854 (2005).

72. Henderson, G. M. & Burton, K. W. Using (234U/238U) to assess diffusion rates of isotope tracers in ferromanganese crusts. *Earth Planet. Sci. Lett.* **170**, 169–179 (1999).

73. Fietzke, J. et al. An alternative data acquisition and evaluation strategy for improved isotope ratio precision using LA-MC-ICP-MS applied to stable and radiogenic strontium isotopes in carbonates. *J. Anal. Spectrom.* **23**, 955–961 (2008).

74. Baker, J., Peate, D., Waight, T. & Meyzen, C. Pb isotopic analysis of standards and samples using a 207Pb-204Pb double spike and thallium to correct for mass bias with a double-focusing MC-ICP-MS. *Chem. Geol.* **211**, 275–303 (2004).

75. Gutjahr, M. et al. Structural limitations in deriving accurate U-series ages from calcitic cold-water corals contrast with robust coral radiocarbon and Mg/Ca systematics. *Chem. Geol.* **355**, 69–87 (2013).

76. Koschinsky, A. & Halbach, P. Sequential leaching of marine ferromanganese precipitates: Genetic implications. *Geochim. Cosmochim. Acta* **59**, 5113–5132 (1995).

77. Glasscock, S. K., Hayes, C. T., Redmond, N. & Rohde, E. Changes in Antarctic bottom water formation during interglacial periods. *Paleoceanogr. Paleoclimatol.* **35**, e2020PA003867 (2020).

78. Hayes, C. T. et al. A stagnation event in the deep South Atlantic during the last interglacial period. *Science* **346**, 1514–1517 (2014).

79. Lu, Z. et al. Oxygen depletion recorded in upper waters of the glacial Southern Ocean. *Nat. Commun.* **7**, 11146 (2016).

80. Yi, L. et al. Plio-Pleistocene deep-sea ventilation in the eastern Pacific and potential linkages with Northern Hemisphere glaciation. *Sci. Adv.* **9**, eadd1467 (2023).

81. Garcia, H. E. et al. Dissolved Oxygen, Apparent Oxygen Utilization, and Oxygen Saturation. *World Ocean Atlas 2013* **3**, 27 (2013).

82. Zweng, M. M. et al. Salinity. *World Ocean Atlas 2013*. **2** (2013).

83. von Blanckenburg, F., O'Nions, R. K. & Heinz, J. R. Distribution and sources of pre-anthropogenic lead isotopes in deep ocean water from FeMn crusts. *Geochim. Cosmochim. Acta* **60**, 4957–4963 (1996).

84. Spratt, R. M. & Lisiecki, L. E. A Late Pleistocene sea level stack. *Clim. Past* **12**, 1079–1092 (2016).

85. Wolff, E. W. et al. Southern Ocean sea-ice extent, productivity and iron flux over the past eight glacial cycles. *Nature* **440**, 491–496 (2006).

86. Lisiecki, L. E. & Raymo, M. E. A Pliocene-Pleistocene stack of 57 globally distributed benthic δ18O records. *Paleoceanography* **20**, https://doi.org/10.1029/2004PA001071 (2005).

Acknowledgements

Author contributions

H.H., M.G., G.K., and J.F. initialized this project. H.H. wrote the first draft of the manuscript with significant inputs from M.G., M.F., C.D.H., X.Z., and J.Y. M.G., C.D.H., and G.K. sampled the crust. H.H. and J.F. performed the laser ablation measurements and data analyses with important inputs from D.L. and J.H. All authors (H.H., J.F., M.G., M.F., G.K., X.Z., C.D.H., D.L., J.H., and J.Y.) contributed to the interpretation of the data and refinement of the manuscript.

Competing interests

The authors declare no competing interests.

Additional information